Nanoscale

Accepted Manuscript

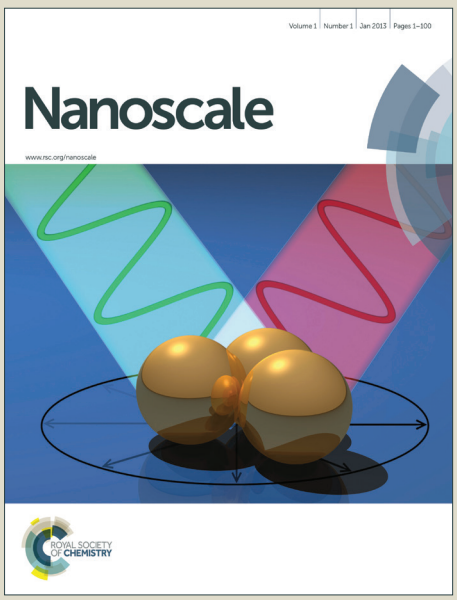

ROYAL SOCIETY OF CHEMISTRY

www.rsc.org/nanoscale

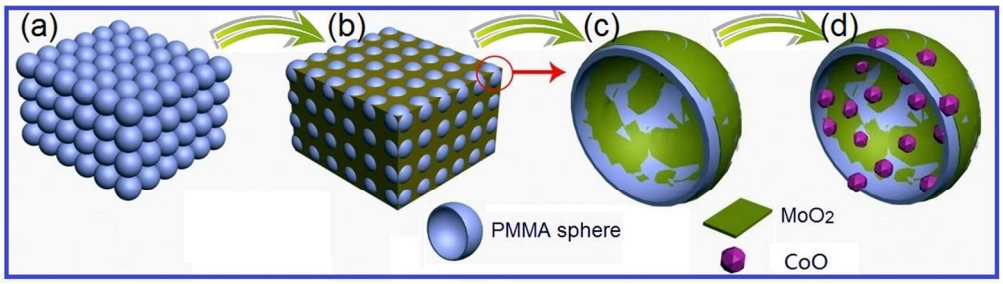

160x44mm (300 x 300 DPI)

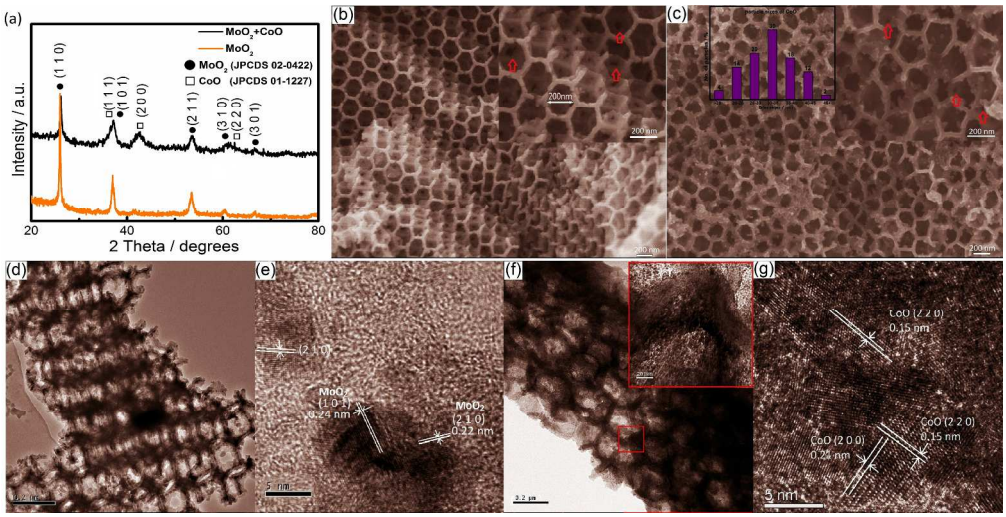

320x162mm (300 x 300 DPI)

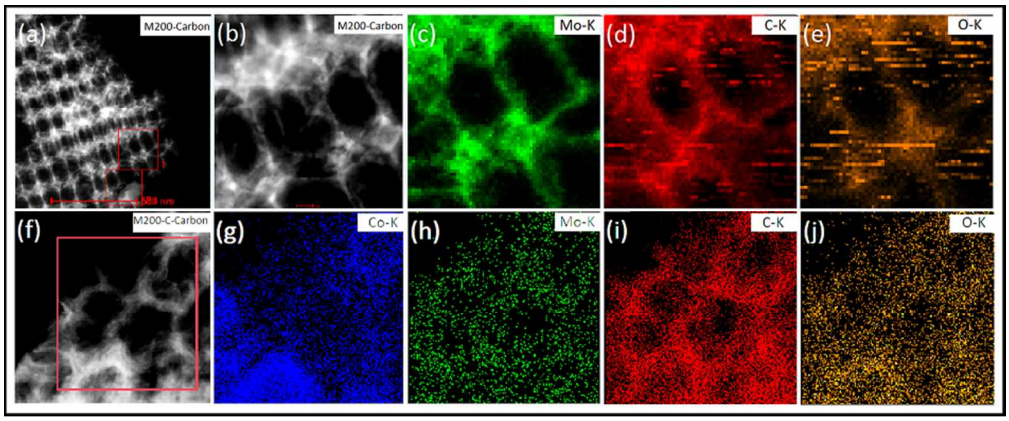

80x32mm (300 x 300 DPI)

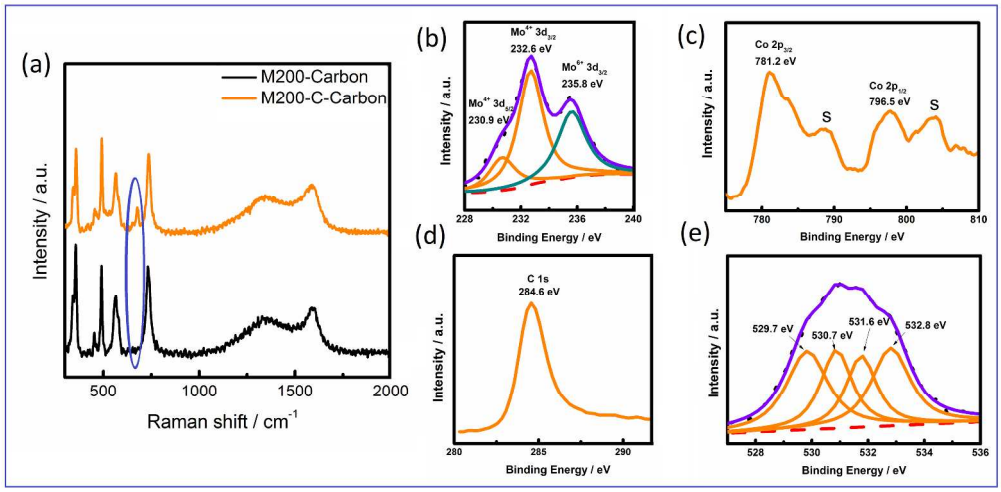

320x158mm (300 x 300 DPI)

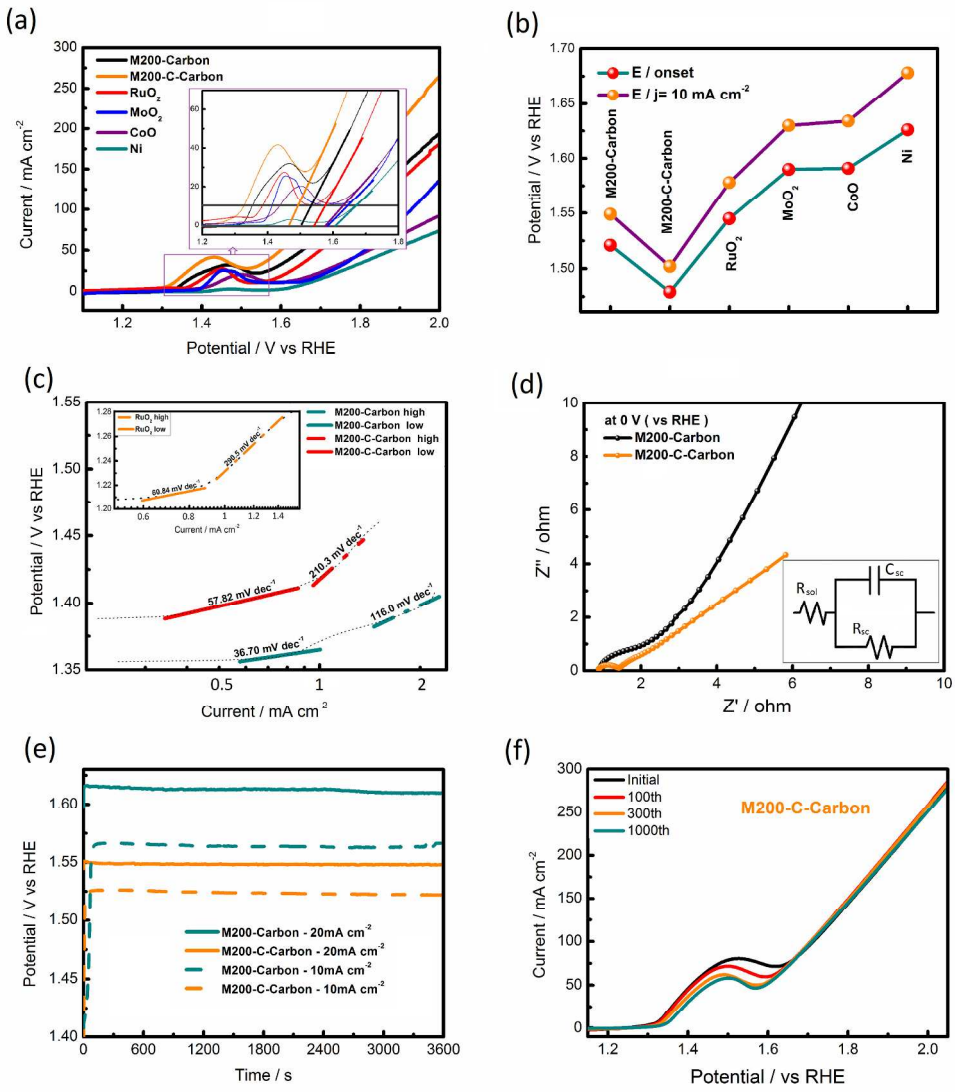

320x356mm (300 x 300 DPI)

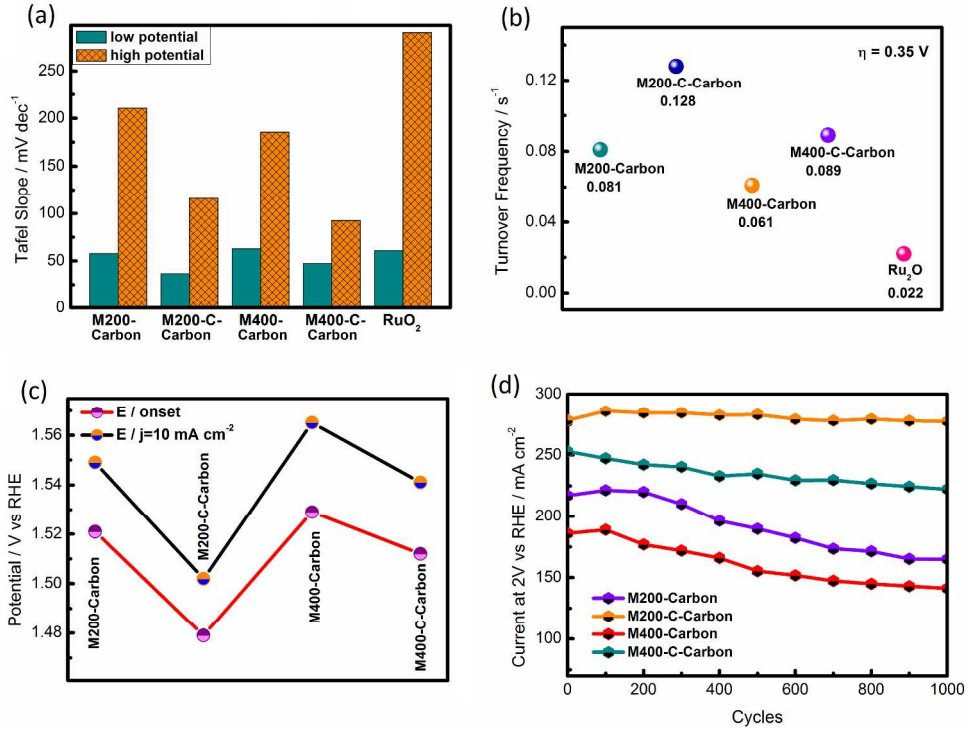

320x239mm (300 x 300 DPI)

MoO_2-CoO coupled with Macroporous Carbon Hybrid Electrocatalyst for Highly Efficient Oxygen Evolution

B. B. Li [a], Y. Q. Liang [a,b] *, X. J. Yang [a, b], Z. D. Cui [a], S. Z. Qiao [a, c]*, S. L. Zhu [a, b], Z. Y. Li [a, b], K. Yin [a,]

[a] School of Materials Science and Engineering, Tianjin University, Tianjin 300072, China

[b] Tianjin Key Laboratory of Composite and Functional Materials, Tianjin 300072, China

[c]School of Chemical Engineering, The University of Adelaide, SA 5005, Australia

Abstract: Cost-effective electrocatalysts for oxygen evolution reactions are attractive for energy conversion and storage processes. A high-performance oxygen evolution reaction (OER) electrocatalyst composed of 3D ordered microporous carbon and MoO_2 skeleton modified by cobalt oxide nanoparticles (MoO_2-CoO-Carbon) is produced through a template method. This unique 3DOM structure finely combines the larger surface area of 3D carbon skeleton and MoO_2 as well as stable anchoring sites for CoO nanocrystals on the skeleton. The synergistic effect between the catalytic activity between MoO_2 and CoO as well as the enhanced electron transport arising from the carbon skeleton contributed to superior electrocatalytic OER properties of MoO_2-CoO-Carbon. The M200-C-Carbon hybrid with overpotential as low as 0.24 V is among the best reported Mo-based OER catalysts. Moreover, the turnover frequency at the overpotential of 0.35 V is 6 times as high as that of commercial RuO_2.

1. Introduction

The growing demand for energy, coupled with the increasing concerns about environment pollution from fossil fuels, has stimulated intense research on clean and

sustainable energy-conversion and -storage systems, such as metal–air batteries, water splitting devices, and fuel cells, As one of the most important process to produce and store renewable energy in chemical form, the oxygen evolution reaction (OER) has led to many studies in recent years. One of the crucial factors limiting efficient water elctrocatalysis is the high overpotential required for the oxygen evolution reaction (OER). [1,2] The activities of noble-metals (Ir, Ru) and transition-metal-based catalysts (Co, Mn, Ni, Fe, etc.) were proposed to be the most active and durable electrocatalysts for OER. [3-5] For the noble-metals, the high cost and element scarcity greatly hindered the widespread use in catalysts. So it becomes more and more urgent to exploit alternative electrocatalysts composed of nonprecious metals or earth-abundant elements that still show high catalytic capability to accelerate the reactions under reduced overpotential. Over the past decade, considerable efforts have been shifted to the development of low-cost 3d transition metal hydroxides/oxides as candidate catalysts for water splitting because of their earth abundance and the relatively low reactivity of unpaired d electrons. [6-9] The transition-metal is supposed to relate to the 3d electron number of the transition metal ions and the surface oxygen binding energy, [10] thus influence their OER activity. Therefore, extensive efforts have been made to use transition-metal based materials as low-cost catalysts or electrode materials for many renewable energy applications. Among these transition-metals, Molybdenum is an important refractory metal. Its oxides mainly include MoO_2 and MoO_3, which have many advance applications as catalysts, catalysis, sensing, electrochromic displays, recording media, electrochemical

* Corresponding author. Tel: +86 22 27402494

E-mail: yqliang@tju.edu.cn

* Corresponding author. Tel: +86 22 27402494

E-mail: s.qiao@adelaide.edu.au

supercapacitors, and field emission due to its efficient charge transport properties. [11-16] However, Molybdenum dioxide (MoO_2), an unusual and attractive transition metal oxide with a distorted rutile structure, was seldom investigated in the OER activities.

To rationally design the reaction interface for an OER, an optimal electrode structure with high specific surface area and better conductivity is essential in improving the energy efficiency. Inorganic nanomaterials with well-defined and uniform pore structures have attracted considerable attention because of their large surface-to-volume ratios, which can increase catalyst/electrolyte contact area and accelerate the diffusion speed so as to enhance the catalytic activity. [17-21] Stucky et. al.[22] synthesized highly ordered mesoporous crystalline MoO_2 materials with diameter of 18 nm by silica template via nanocasting strategy. Template-directed method is a promising candidate for enhancing the specific activity for OER. It is because that template-directed synthesis is an ideal approach to replication for the fabrication of inorganic materials with controllable structural properties. [23-25] Various templates were selected to fabricate the porous structure. Here, we choose poly-(methyl methacrylate) (PMMA) colloidal crystals as templates due to its perfect wettability with polar solvents (such as H_2O and alcohol).[26]

The size of the pheres can be controled by the amout of methyl methacrylate in the process of preparation.[27] In this paper, we introduce porosity into MoO_2 and use PMMA colloidal crystal template to prepare three-dimensionally ordered macroporous (3DOM) MoO_2. Significantly, when Mo precursor integrating PMMA template was calcined under N_2 protection, the PMMA templates was partially removed, leaving three-dimensionally ordered carbon skeleton. The MoO_2 crystalline were distributed uniformly on the surface of carbon skeleton. As a result, the residual 3D carbon skeleton can intensely improve the conductivity of 3DOM structures. In addition, OER with high activity and strong long-term stability is also urgently needed. However, 3DOM MoO_2-Carbon having ordered carbon skeleton used as continuous pathway for electron transport do not possess sufficient active sites for

further OER improvement. Therefore, further improvement of this type of electrode is highly desirable, especially through elemental doping or through introducing other transition-metal oxide into 3DOM MoO_2-Carbon. It has been reported that compounds of earth-abundant cobalt (for example Co_3O_4) exhibit better OER activity. However, the easy accumulation of pure Co_3O_4 decreases the active sites and hampers the transport of electrons or protons during the oxidation process [28-31]. The spinel-type cobalt oxide (CoO) exhibits various interesting electrochemical and catalytic properties due to their good catalytic activity and corrosion stability toward electrochemical OER in alkaline media. [32-35] In order to provide more active sites, CoO was successfully introduced in 3DOM MoO_2-Carbon, and forming 3DOM hybrid MoO_2-CoO-Carbon in the first time. 3DOM MoO_2-CoO-Carbon is expected to give excellent OER performance, because rich active sites and high electron conductivity are combined. Moreover, the rich pores in 3DOM MoO_2-CoO-Carbon can provide high surface area and multidimensional mass transport pathways during electrochemical processes, which are highly advantageous to achieve the desired electrocatalytic OER performance for noble-metal-free catalysts and an excellent durability.

2. **Results and Discussion**

The fabrication process for 3DOM MoO_2-CoO-Carbon is demonstrated in Figure 1 First, 3D PMMA colloidal crystals was obtained by self-organization (Figure 1a and Figure S1a,b). Next, $MoCl_5$ precursor was poured into the self-assembled PMMA colloidal. This solution will easily permeate through the interface of PMMA spheres (Figure 1b). The interstices of the colloidal crystals are then filled with the solution and subsequently dried at a certain temperature. Then, the as-dried sample is placed into a furnace at N_2 atmosphere to burn off the PMMA spheres and meanwhile form a homogeneous metal-oxide thin film (Figure 1c). Notably, the PMMA spheres were not removed completely, leaving three-dimensionally ordered carbon skeleton modified by MoO_2 thin film (3DOM MoO_2-Carbon). After dispersing in $Co(NO_3)_2$

precursor and annealing treatment, 3DOM MoO_2-Carbon were further modified by CoO nanoparticles (3D MoO_2-CoO-Carbon in Figure 1d, Figure S1c-f and Figure S2).

The structure and morphology of as-prepared 3D MoO_2-Carbon and MoO_2-CoO-Carbon (with diameter of 200 nm, denoted as M200-Carbon and M200-C-Carbon) were investigated by means of X-ray diffraction (XRD), scanning electron microscopy (SEM) and transmission electron microscopy (TEM). The XRD pattern confirmed the formation of MoO_2 with tetragonal structure patterns and CoO nanoparticles (Figure 2a). But no typical peak of carbon was indexed due to the amorphous structure. Because of the influence of the amorphous carbon, MoO_2 diffraction peaks are not particularly sharp (orange line). Moreover, the full width at half maximum (FWHM) of the diffraction peak increases due to the existence of CoO (black line). SEM images revealed a long-range ordered hemispheroidal arrangement of inverse opal nanostructure in Figure 2b,c and Figure S1c,d. The average center-to-center distances between two macropores in the 3DOM MoO_2-CoO-Carbon and MoO_2-CoO-Carbon are all about 200 nm, which is shorter than the average distances (around 280 nm) between two PMMA spheres (Figure S1a). This indicates that the pores shrunk by 29% upon calcination. This shrinkage is caused by the melting of polymer templates and the sintering of the produced metal oxides. Nevertheless, the long-range orderly and uniform pore structures of the 3DOM MoO_2-Carbon are not destroyed by this large shrinkage. After CoO modification, some small particles with the average diameter of 30 nm can be seen on the skeletons of MoO_2-Carbon in Figure 2c. Some connecting channels (marked by red arrows) in the macropore formed by the contact of the template spheres can be seen in Figure 2b,c. These channels connected macropores are favorable for internal part of 3DOM materials to exchange substance outside. To get more detail information on the 3DOM MoO_2-Carbon and MoO_2-CoO-Carbon, TEM images are presented in Figure 2d-g. The wall thickness of the 3DOM MoO_2-Carbon is in range of 20-30 nm. Some lattices distribute on the amorphous carbon matrix uniformly. By comparing the lattice spacings (d values) of the 3DOM MoO_2-Carbon with that of standard MoO_2

sample, it appears that the (1 0 1) and (2 1 0) planes of the MoO_2 are exposed. Figure 2f,g show the particles of CoO deposited on the of M200-Carbon skeletons, whose average size is around 30 nm. By measuring the interplanar spacing, it appears that the (2 0 0) and (2 2 0) planes of the CoO are exposed. The samples of 3DOM MoO_2-Carbon and MoO_2-CoO-Carbon with diameter of 400 nm (denoted as M400-Carbon and M400-C-Carbon) were also synthesized for comparison, as shown in Figure 3S.

Furthermore, the corresponding EDS mapping analyses of M200-Carbon (Figure 3a-e) reveal the homogeneous distribution of molybdenum, carbon, and oxygen in the whole 3DOM structures. The results of M200-C-Carbon (Figure 3f-j) and M400-C-Carbon (Figure S4) prove that CoO particles load on the amorphous carbon skeletons uniformly. These results are consistent with the previous argument.

In order to study the MoO_2 coated on conductive carbon structure before and after CoO modification, the Raman spectra test was carried out. The carbon structure is closely related to the graphitization degree. Figure 4a shows the Raman spectra of the samples M200-Carbon and M200-C-Carbon respectively. Both Raman spectra consist of two broad bands at 1356 and 1591 cm^{-1}, which can be ascribed to the characteristic Raman spectra of carbon. The former can be assigned to sp^{3-} hybridized disordered carbon or defective carbon (D-band), and the latter is associated with the sp^{2-} hybridized graphitic carbon (G-band). [36,37] The relative intensity of I_D / I_G reflects the ratio of disordered carbon to graphitic carbon. The calculated value of I_D / I_G is about 0.81, suggesting that the pyrolysis product is not purely graphitic carbon, instead contains large amounts of amorphous carbon. We can observe that the spectrum of M200-Carbon is constituted by several peaks located at 346, 350, 496, 588, and 744 cm^{-1}, which are in good agreement with the spectrum of MoO_2 reported. [38,39] Compared with M200-Carbon, M200-C-Carbon has an additional peak of located at 686 cm^{-1} (marked by blue circle) corresponding to the vibration modes of CoO. [40,41] This results demonstrate the existence of well-crystallized CoO. XPS was used to determine the surface compositions of the M200-Carbon and M200-C-Carbon (Figure

S5 and Figure 4b-e). High-resolution XPS spectra of Mo 3d (Figure 4b) were deconvoluted into 3 peaks according to the oxidation and surface electronic states of Mo, corresponding to the MoO_2 along with small amount of MoO_3. MoO_3 may result from the slight surface oxidation of metastable MoO_2 in air. [42, 43] The presence of pure CoO in Figure 4c was confirmed by the intense shake-up satellites 6 eV above the primary spin-orbit BEs. The spectra of O1s further confirm the existence of CoO (529.7 eV), MoO_2 (530.7 eV), and MoO_3 (531.6 eV), and the peak at approximately 532.2 eV is attributed to physisorbed water. The C1s pattern is assigned to C^0 of carbon skeleton.

To better characterize the formation mechanism of product, TGA and DTA measurements under Argon and air atmosphere are performed. The changes occurred in the MoO_2 sample can be described according to the two zones marked in the Figure 5 In zone I, negligible weight loss can be observed during the heating process from room temperature to 300 °C, while significant weight losses of 70% in Argon and 90% in air emerge at 300-400°C. (Thus the content of carbon in M200-Carbon composites is estimated to be 66.6%). This is caused by the phenomenon that the PMMA thermal decomposition, remaining an amount of amorphous carbon skeletons in Argon atmosphere. But only small amount of carbon skeleton has been left because a majority of PMMA was decomposed under air condition. Notably, an obvious endothermal peak emerges at 370 °C, revealing the transition from MoO_3 to MoO_2. The existence of MoO_3 was proved by the XRD pattern for the PMMA templates after treated by $MoCl_5$ precursor but without calcinations (Figure S6a). As the formation of MoO_2, C steam produced from heating PMMA colloidal crystals may play a major role. The associated chemical reaction can be listed as follows:

$$MoO_3 + C \rightarrow MoO_2 + CO$$

In zone II (410–650°C), there is another endothermic peak at 465 °C in the DTA curve under Argon atmosphere, but no peak appears under air. This peak in 465 °C is due to the fact that the m-MoO_2 sample has been transformed to the

thermodynamically stable phase of molybdenum oxide, a-MoO_3. Simultaneously, the morphology of the as-formed product changed from into plate-like structure in Figure S6b.

Electrocatalytic properties of the 3D MoO_2-CoO-Carbon hybrid were investigated with respect to OER in a typical three electrode configuration in 1M KOH. Ni foam uniformly coated with the as-synthesized 3D MoO_2-CoO-Carbon hybrid was used as the working electrode. For comparison, four reference samples were also tested under otherwise identical conditions, including RuO_2, which was previously reported to be an advanced electrode material, [44,45] commercial MoO_2, 3D CoO, and Ni foam. The iR-corrected linear sweep voltammetry (LSV) curves of OERs for the set of catalysts are shown in Figure 6a. Apart from an additional electron-transfer process at around 1.38 V, which can be assigned to the NiII/NiIII or IV redox couple, several features are worth noting. First, the Ni foam shows negligible OER response, as shown in the LSV curve conducted in 1M KOH solution. The CoO (coated on Ni foam with the same synthesis method, presenting porous structures in the Supporting Information) and commercial MoO_2 also displays slight higher OER response than Ni foam with a high onset potential at about 1.63 V vs the reversible hydrogen electrode (RHE; Figure 6a), Noticeably, the anodic current recorded on M200-Carbon exhibits the lower onset potential at approximately 1.52 V, which suggests better catalytic activity due to the 3DOM structures. Second, M200-C-Carbon is reckoned to be the most active catalyst among these samples, rendering a sharp onset potential at 1.47 V with greatly enhanced OER current. This clearly indicates that the coupling of two components (3D M200-Carbon and CoO) can significantly improve the catalytic activity. Moreover, the OER current of M200-C-Carbon largely exceeds that of RuO_2. The operating potentials (versus RHE) to deliver a 10 mA cm^{-2} current density were compared in Figure 6b, which is a metric related to solar fuel synthesis. [46, 47]

Here are OER catalysts of 3D M200-C-Carbon hybrid, 3D M200-Carbon, 3D CoO, commercial MoO_2, RuO_2, and Ni, the corresponding potentials of which at 10 mA cm^{-2} were 1.50, 1.55, 1.63, 1.63, 1.58, and 1.68 V, respectively (Figure 6b). Several

remarks on the result are required. First, for the OER catalysts of 3D MoO_2-Carbon-CoO, a lower voltage was required to achieve 10 mA cm^{-2}, and the voltage values is much lower than that of noble metal oxide OER catalysts (RuO_2). Second, the value of 3D M200-C is comparable to that of RuO_2, indicating that the porous MoO_2-C possesses as high ORR activity as noble metal oxide. Finally, the activity of the 3D M200-C-Carbon hybrid catalyst is the highest among the samples we prepared in this work, and this confirms that the synergetic effect arising from the interactions between MoO_2 and CoO could improve the electrocatalytic performance. Moreover, this excellent OER activity of 3D M200-C-Carbon is not only better than that of most of transition-metal electrocatalysts and nonmetal catalysts but also superior to that of all the porous electrodes reported to date [48-52]: $ZnxCo_{3-x}O_4$ nanowire arrays grown on Ti foils (1.55 V, pH 14), $Ni_xCo_{3-x}O_4$ nanowire arrays grown on Ti foils (1.60 V, pH 14), Ni-substituted Co_3O_4 nanowire arrays grown on Ni foams (1.60 V, pH 14), Au@Co_3O_4 catalyst (1.58 V, PH 13), Co_3O_4 nanoparticles grown on reduced mildly oxidized graphene oxide (Co_3O_4/rmGO 1.54V, PH 13), $Fe_2(MoO_4)_3$ grown on Ni foams (1.51 V, pH 14). A detailed comparison of different highly active OER catalysts with various electrode configurations is shown in Table S1, further confirming the outstanding catalytic behavior of M200-C-Carbon.

To shed light on the origin of the synergistic effect and the intrinsic advantage of this advanced hybrid material, the catalytic kinetics of these samples for the OER was examined by Tafel plots (Figure 6c). Two distinct linear regions at both low and high over potentials were presented in the Tafel plots. In the low over potential region, the overall OER process is controlled by the kinetics of the surface reactions, [53] while in the high over potential region, the reaction speed is dominated by the diffusion limitations inside the material. The Tafel slope of 3D M200-Carbon is comparable to that of RuO_2, but the slope of M200-C-Carbon with the lowest value of 36.70 mV dec^{-1} is much lower than that of RuO_2 in low over potential region. Similarly, the slopes of 3D M200-C-Carbon and 3D M200-Carbon in high over potential region also

give the lower values (116.0 mV dec^{-1} and 210.3 mV dec^{-1}) than that of RuO_2(290.5 mV dec^{-1}).

Also, the semicircular diameter in the electrochemical impedance spectrum (EIS) of 3D M200-Carbon is much larger than that of 3D M200-C-Carbon, due to smaller contact and charge transfer impedance in 3D M200-C-Carbon (Figure 6d). As the cobalt oxide particles with good crystallinity can improve the electrical conductivity of the whole structure, its addition was also beneficial to decrease the charge transfer resistance. The Tafel and EIS results indicate that 3D M200-C-Carbon possesses best catalytic activity which is provoked by facilitated electron transfer. Other than high OER activity, the durability of electrocatalysts is another important parameter, as it determines the cycle life. Chronopotentiometry (it) measurements were carried out at a constant anodic current density of 10 mA cm^{-2} and 20mA cm^{-2} (Figure 6e). Both M200-Carbon and M200-C-Carbon exhibited high OER stability with no significant activity loss over 1 h.

A stable catalytic performance in high concentration alkaline solutions is critical for realistic applications. [54] The M200-C-Carbon maintained nearly the same OER onset potentials and the similar LSV curve by performing continuous LSV for 1000 cycles (Figure 6f), suggesting the excellent durability during long-term cycling. As the increase of reaction laps, Ni oxidation peak is gradually reduced, and only slight degradation can be observed between the curves measured at the initial cycle and after 1000 cycles. This insignificant activity decrease may be caused by a small mass loss of the catalyst due to its partial peeling by a large amount of the evolved oxygen. The high OER activity and durability of this electrocatalysts were attributed to the strong coupling effect between nanoscale active CoO particles and conducting amorphous carbon phase coupled by MoO_2. Their 3DOM structures are conducive to eliminate the negative effects, such as volume strain. Coordinate to consider these two factors, M200-C-Carbon may have the best performance.

The OER activity of M400-Carbon and M400-C-Carbon was also examined in the same way. Figure S7b shows the LSV electrochemical impedance spectroscopy for M400-Carbon and M400-C-Carbon. To assess the effect of pore size of 3D MoO_2 on the OER activity, the onset potential, Tafel slope, charge-transfer resistance values, are listed in Table S2. Within the catalyst series, the OER activity increased in the order of M400-Carbon < M200-Carbon < M400-C-Carbon < M200-C-Carbon, indicating two notable remarks. On the one hand, CoO nanoparticles play an important role in improving 3D MoO_2 in both sizes of samples (M200-Carbon and M400-Carbon). Tafel and EIS results for M400-Carbon and M400-C-Carbon in Figure S7 (c,d) further confirm this results. On the other hand, 3D MoO_2 with larger pore size displays lower OER activity than that of smaller pore size. The Nyquist plots reveal a remarkable decrease of the charge transfer resistance (RCT) from 34.9 Ω (M400-Carbon) to 2.8 Ω (M200-Carbon), which can be attributed to the average volume structure. To compare the different durability of the M400-Carbon and M400-C-Carbon, chronopotentiometry curves of these samples were examined under high current densities of 10 and 20 mA cm^{-2} (Figure S7e). Both of the two samples display excellent stability during the first 60 minutes.

The unique hybrid hierarchical pore architectures endow M200-C-Carbon and M400-C-Carbon with catalytic performance much better than that of conventional electrode materials. The catalytic kinetics of these samples (M200-Carbon, M200-C-Carbon, M400-Carbon, and M400-C-Carbon, RuO_2) for the OER examined by Tafel slopes located at both low and high over potentials were presented in Figure 7a The overall OER process is controlled by the kinetics of the surface reactions in the low over potential region, while the reaction speed is dominated by the diffusion limitations inside the material in the high over potential region. Within the catalyst series, the Tafel slope at low over potentials increased in the order of M200-C-Carbon (36.70 mV dec^{-1})<M400-C-Carbon (47.39 mV dec^{-1})<M200-Carbon (57.82 mV dec^{-1})<RuO_2 (60.84 mV dec^{-1}) <M400-Carbon (62.73 mV dec^{-1}). Impressively the estimated Tafel slopes of M200-Carbon and M400-Carbon are close to RuO_2, but the

Tafel slopes of M200-C-Carbon and M400-C-Carbon are much lower than that of RuO_2. This demonstrates that introducing CoO can provide the large number of active sites, facilitating electron transfer by the native carbon skeleton. The enhanced OER performances benefit from the synergistic effect between MoO_2 (large surface area) and CoO (good electric conductivity, SI Figure S8), which allow the faster ion diffusion and electron transport at electrode/electrolyte interface. This facile design and rational synthesis offers an effective strategy to enhance the electrochemical performance of OER and shows promising potential for hydrogen splitting.[55] Furthermore, electrochemical double layer capacitances (C_{dl}) measured to evaluate the effective surface area of various catalysts (SI Figure S9). M200-C-Carbon exhibits much larger than M200-Carbon indicating the high exposure of effective active sites, which is responsible for the excellent OER activity. The Brunauer–Emmett–Teller (BET) surface areas and adsorption behaviors over MB of the catalysts were measured, as shown in Figure S10,11 The M200-Carbon and M200-C-Carbon catalysts show a larger BET surface area than M400-Carbon and M400-C-Carbon, providing more active sites for OER. Moreover, the M200-C-Carbon catalyst has a smaller BET surface area but a higher catalytic activity than M200-Carbon, further confirming the excellent catalytic performance of the CoO participating in OER. The electroactive surface areas of the the catalyst series were estimated by the cyclic voltammetry method. From Figure S13, the peak current increased linearly with the square root of the scan rate, indicating a quasi-reversible diffusion controlled process [56]. From Randles–Sevcik equation (eq 3, supporting information), the electroactive surface area of the catalysts is directly proportional to the slope. The higher the slope indicates the larger electroactive surface area. As shown in Figure S13e, the slope increased in the order of M400-Carbon (8.8) < M200-Carbon (10.7) < M400-C-Carbon (11.8) < M200-C-Carbon (13.1), suggesting the electroactive surface area increasing in the same order. This result is totally accordance with the LSV of Figure 7b. Similarly, the Tafel slope at high over potentials increased in the order of M400-Carbon (92.45 mV dec^{-1}) < M200-C-Carbon (116.0 mV dec^{-1}) < M400-Carbon (185.4 mV dec^{-1}) < M200-Carbon (210.3 mV dec^{-1}). The lower Tafel slope

corresponds to fast mass transfer inside this 3D porous material. M400-Carbon and M400-C-Carbon possess larger ordered macropores than that of M200-Carbon and M200-C-Carbon, and larger macropores facilitated mass transfer through transmission channel inside the 3D porous structures. Remarkably, CoO modification also plays a positive effect on improving mass transfer.

The OER activities of the different electrodes were evaluated at a potential of 1.58 V (η = 350 mV). The currents obtained at this potential were converted to turnover frequencies (TOFs). It should be pointed out that the as calculated TOFs could be gross underestimations of the actual TOFs because not every metal atom could be catalytically active. Moreover, it is worth noting that the TOF values of the M200-C-Carbon hybrid is much higher than the other three catalysts and is almost 6 times as high as that for RuO_2. Therefore, the TOF result lends further support to the conclusion that the advanced catalytic performances of the M200-C-Carbon on OER is derived from the strong interactions between the M200-Carbon hydroxide layers and the CoO nanoparticles at the molecular level. We further compared the onset potentials and operating potentials required for different catalysts to deliver a 10.0 mA cm^{-2} current density ($E_{j=10\ mA\ cm\text{-}2}$). M200-C-Carbon exhibits the lowest onset potential, and affords a current density of 10.0 mA cm^{-2} at the lowest applied potential. Catalyst durability is another major challenge for OER. The best stability under continuous OER process is identified for M200-C-Carbon, as shown in Figure 7d, plots of current density at η= 350 mV versus the cycling numbers. It can be seen that negligible degradations are observed for M200-C-Carbon and M400-C-Carbon for current cycling up to 1000 cycles, suggesting the superior stability of the CoO modified 3D MoO_2-Carbon. CoO nanocrystals are locally crystallized and grown on the surface of MoO_2 inner wall of micropores, leading to a super-stable hybrid structure. Therefore, the loss of the 3D MoO2-CoO-Carbonduring the durability test is trivial [57]. In sharp contrast, M200-Carbon and M400-Carbon possess relatively poor long-term stability, which can be attributed to the relatively large solubility in alkaline medium owing to the poor crystallinity of MoO_2. [58]

4. Conclusion

In summary, we have demonstrated a high-performance OER electrocatalyst composed of 3D MoO_2-CoO-Carbon hybrids. The unique 3D ordered miroporous structure offers a large surface area and stable anchoring sites for CoO nanocrystals. Owing to the large surface area of M200-Carbon and synergistic effect between MoO_2 and CoO, the M200-C-Carbon exhibits enhanced OER activity (a high negative onset potential and a small Tafel slope at low potential region), that is much higher than that of a commercial RuO_2 and excellent durability in an alkaline electrolyte. At overpotential of 0.35 V, M200-C-Carbon has a TOF value 6 times as high as RuO_2. The novel MoO_2-CoO-Carboncatalyst offers radically new opportunities for developing next-generation OER processes with carbon and non-precious metal-based materials, and thus is believed to be a promising candidate for water splitting applications.

Experimental Section

Fabrication of 3DOM MoO_2-CoO-Carbonsamples

All chemicals (purity of 99.9%) used in this research were of research purity and used without further purification. The PMMA colloidal crystal template assembled by PMMA spheres with average diameter of 280 nm and 450 nm was synthesized by literature techniques.[59] Though adding different amount of methyl methacrylate, we can get different sizes of PMMA spheres In the process of preparation. The PMMA spheres were dispersed in water by sonication, reaching a concentration up to 0.025 g mL^{-1}, then the solution were poured into a watch-glass to obtain the self-organized 3D PMMA colloidal crystals after evaporation of moisture at 40 °C. A typical procedure is shown as follows: 0.137 g $MoCl_5$ was dissolved in 5 ml of distilled water with slow stirring at room temperature until the nitrate salt dissolved completely.

Then the PMMA colloidal crystals were poured into the solution and soaked in the solution at 50 °C for 24 h in air. After the PMMA colloidal crystals became dark blue (Molybdenum has been oxidized), excess solution was removed from the impregnated PMMA colloidal crystals by vacuum filtration. The obtained sample was allowed to dry in air at room temperature overnight, and then calcined in a tubular furnace in an N_2 flow. The temperature was raised at a rate of 8 °C/min to 650 °C and held for 1.5 h. The samples were cold under the protection of N_2. Due to the different pore sizes, the two kinds of black samples were marked as M200-Carbon and M400-Carbon respectively. To load CoO nanoparticles on the 3DOM MoO_2-Carbon skeletons, the as-formed black samples were dispersed into the 4 ml water and ethylene glycol (EG) with 2 g $Co(NO_3)_2$ for 24 h in air. Excess solution was removed from the impregnated PMMA colloidal crystals by vacuum filtration. After drying at 60 °C for 5 h, black powders were calcined at 350 °C for 2 h in vacuum. These samples with different pore sizes were marked as M200-C-Carbon and M400-C-Carbon respectively.

Physical characterization

The morphology and structure of samples were characterized by transmission electron microscopy (TEM, Philips Tecnai G2 F20), atomic force microscopy (AFM, Nanoscope III), and X-ray diffraction (XRD, RIGAKU/DMAX). Surface chemical analysis of MoO_2-Carbon and MoO_2-CoO-Carbonwere performed by X-ray photoelectron spectroscopy (XPS) using a PHL1600ESCA instrument equipped with a monochromatic Mg Ka X-ray source (E = 1253.6 eV) source operated at 250 W. The Raman spectra were collected by using DXR Microscope (Thermo Electron Corporation). Surface chemical analysis of MoO_2-Carbon and MoO_2-CoO-Carbon were performed by X-ray photoelectron spectroscopy (XPS) using a PHL1600ESCA instrument equipped with a monochromatic Mg Ka X-ray source (E = 1253.6 eV) operating at 250 W. The spectra obtained with 532 nm were practically identical. The N_2 sorption test was characterized by automated gas sorption analyzer (Quantachrome AsiQOV002-4). The nitrogen adsorption–desorption isotherms were measured at -196 °C with a Gemini VII surface area and porosity system. The specific surface area

was estimated by the Brunauer–Emmett–Teller (BET) method, and the pore size was calculated by the Barrett–Joyner–Halenda (BJH) method using the adsorption branch of the isotherms. Thermogravimetric analysis (TGA) and differential thermal analysis (DTA) were performed on a SDTQ600 (TAInstruments) TG-DTA Analyzer in air.

Electrochemical Characterization

All of the electrochemical measurements were performed in a three-electrode system on an electrochemical workstation (Gamry Reference 600). The working electrodes prepared by mixing the catalysts samples, acetylene black, and poly (vinyldifluoride) (PVDF) at a weight ratio of 70:15:15, were pasted on pure Ni foam, and was immersed into 1 M KOH solution. The geometric area of Ni foam immersed in the solution was used to calculate the current density. An Ag/AgCl electrode was used as the reference electrode and a Pt wire was used as the counter electrode. The reference was calibrated against and converted to reversible hydrogen electrode (RHE). Linear sweep voltammetry (LSV) was carried out at 25 mV s^{-1} for the polarization curves and 1 mV s^{-1} for Tafel plots. The catalysts were cycled about 5 times of cyclic voltammetry (CV) until a stable CV curve was developed before measuring polarization curves of catalysts. Chrompotentiometry (CP) was carried out under a constant current density of 10 mA cm^{-2} and 20 mA cm^{-2}. The Nyquist plots were measured with frequencies ranging from 100 kHz to 0.1 Hz at an overpotential of 250 mV. The impedance data were fitted to a simplified Randles circuit to extract the series and charge-transfer resistances. The conversion of Ag/AgCl reference electrode to the reversible hydrogen electrode (RHE),[60] the applied external potential and the effect of pH of electrolyte can be converted into the potential vs. RHE: $E_{RHE}=E_{(vs.\ Ag/AgCl)} + E_{AgCl} + 0.059$ pH, where $E_{AgCl} = 0.197$ V at 25 °C. For example, when the $V_{bias} = 0$ V (vs. Ag/AgCl) at pH electrolyte, V_{bias} (V vs. RHE) = 0 + 0.197 + 0.059 × 14 = 1.027 V.

Acknowledgments

Financial supports by National Natural Science Foundation of China (51402211) and Natural Science Foundation of Tianjin (15JCQNJC03600) are gratefully acknowledged.

References

[1] Z. B. Zhuang, W. C. Sheng, Y. S. Yan, Adv. Mater. 2014, 26, 3950 – 3955.

[2] X. Long, J. K. Li, S. Xiao, K. Y. Yan, Z. L. Wang, H. N. Chen, S. H. Yang, Angew. Chem. Int. Ed. 2014, 53, 7584 – 7588.

[3] J. J. Concepcion, J. W. Jurss, M. R. Norris, Z. Chen, J. L. Templeton, T. J. Meyer, Inorg. Chem. 2010, 49, 1277– 1279.

[4] L. Duan, F. Bozoglian, S. Mandal, B. Stewart, T. Privalov, A. Llobet, L. Sun, Nat. Chem. 2012, 4, 418 – 423.

[5] N. D. McDaniel, F. J. Coughlin, L. L. Tinker, S. Bernhard, J. Am. Chem. Soc., 2008, 130, 210 – 217.

[6] X. Zou, A. Goswami, T. Asefa. J. Am. Chem. Soc. 2013, 135, 17242 – 17245.

[7] C. C. L. McCrory, S. Jung, J. C. Peters, T. F. Jaramillo. J. Am. Chem. Soc. 2013, 135, 16977 – 16987.

[8] M. Gong, W. Zhou, M. C. Tsai, J. G. Zhou, M. Y. Guan, M. C. Lin, B. Zhang, Y. F. Hu, D. Y. Wang, J. Yang. Nat. Commun. 2014, 5, 4695 - 4700.

[9] P. S. Matsumoto. J. Chem. Educ., 2005, 82, 1660 - 1661.

[10] I. C. Man, H. Y. Su, F. Calle-Vallejo, H. A. Hansen, J. I. Martinez, N.G. Inoglu, J. Kitchin, T. F. Jaramillo, J. K. Norskov, J. Rossmeisl, ChemCatChem. 2011, 3, 1159 – 1165.

[11] S. C. Hou, G. H. Zhang, W. Zeng, J. Zhu, F. L. Gong, F. Li, H. G. Duan, ACS Appl. Mater. Interfaces 2014, 6, 13564 − 13570.

[12] S. Hu, F. Yin, E. Uchaker, W. Chen, M. Zhang, J. Zhou Y. Y. Qi, G. Z. Cao, J. Phys. Chem. C 2014, 118, 24890 − 24897.

[13] Z. X. Huang, Y. Wang, Y. G. Zhu, Y. M. Shi, J. I. Wong. H. Y. Yang, Nanoscale. 2014, 6, 9839 - 9845.

[14] Z. W. Xu, H. L. Wang, Z. Li, A. Kohandehghan, J. Ding, J. Chen, K. Cui, D. Mitlin, J. Phys. Chem. C 2014, 118, 18387−18396.

[15] C. Liu, Z. C. Li, Z. J. Zhang, Electrochim. Acta 2014, 134, 84 – 91.

[16] Q. Yang, Q. Liang, J. Liu, S. Q. Liang, S. S. Tang, P.J. Lu, Y.K. Lu, Mater. Lett. 2014, 127, 32 – 35.

[17] B. Rajesh, Z. Piotr, Nature 2006, 443, 63 - 69.

[18] W. Z. Li, C. H. Liang, W. J. Zhou, J. S. Qiu, Z. H. Zhou, G. Q. Sun, Q. Xin, J. Phys. Chem. B 2003, 107, 6292-6299.

[19] Y. G. Li, W. Zhou, H. L. Wang, Nat. Nanotechnol. 2012, 7, 394 - 400.

[20] Z. S. Wu, A. Winter, L. Chen, Y. Sun, A. Turchanin, X.L. Feng, K. Müllen, Adv. Mater. 2012, 24, 5130 – 5135.

[21] A. Vin, C. Streb, V. Murugesan, M. Hartmann, J. Phys. Chem. B 2003, 107, 8297 -- 8299.

[22] Y. F. Shi, B. K. Guo, S. A. Corr, Q. H. Shi, Y. S. Hu, K. R. Heier, L. Q. Chen, R. Seshadri, G. D. Stucky, Nano Lett. 2009, 12, 4215 – 4220.

[23] J. Liang, X. Du, C. Gibson, X. W. Du, S. Z. Qiao. Adv. Mater. 2013, 25, 6226 – 6231.

[24] R. L. Liu, D. Q. Wu, X. L. Feng, K. Müllen, Angew. Chem. Int. Ed. 2010 , 49 , 2565 - 2569.

[25] J. Liang, Y. Jiao, M. Jaroniec, S. Z. Qiao, Angew. Chem. Int. Ed. 2012, 51, 11496 – 11500.

[26] H. W. Yan, C. F. Blanford, J. C. Lytle, C. B. Carter, W. H. Smyr, A. Stein. Chem. Mater. 2001, 13, 4314-4321.

[27] S. L. Wanga, Z. X. Zhanga, S. H. Fanga, L.Yanga, C. C. Yangb, S. Hiranoc. Electrochim. Acta. 2013, 111, 685– 690.

[28] A. J. Esswein, M. J. McMurdo, P. N. Ross, A. T. Bell, T. D. Tilley. J. Phys. Chem. C 2009, 113, 15068 – 15072.

[29] J. Zhao, Y. Zou, X. Zou, T. Bai,Y. Liu, R. Gao, D. Wang, G. D. Li, Nanoscale 2014, 6, 7255 - 7262.

[30] H. Tueysuez, Y. J. wang, S. B. Khan, A. M. Asiri, P. Yang. Nano Res. 2013, 6, 47 - 54.

[31] J. A. Koza, Z. He, A. S. Miller, J. A. Switzer. Chem. Mater. 2012, 24, 3567 – 3573.

[32] Y. Liang, Y. Li, H. Wang, J. Zhou, J. Wang, T. Regier, H. Dai, Nat. Mater. 2011, 10, 780 – 786.

[33] B. S. Yeo, A. T. Bell, J. Am. Chem. Soc. 2011, 133, 5587 – 5593.

[34] J. B. Gerken, J. G. McAlpin, J. Y. C. Chen, M. L. Rigsby, W. H. Casey, R. D. Britt. S. S. Stahl, J. Am. Chem. Soc. 2011, 133, 14431 – 14442.

[35] F. Jiao. H. Frei, Energy Environ. Sci. 2010, 3, 1018 – 1027.

[36] X. Zhao , C. Hu , M. Cao , Chem. Asian J. 2013 , 8 , 2701 – 2707 .

[37] Z. Wang , T. Chen , W. Chen , K. Chang , L. Ma , G. Huang , D. Chen , J. Y. Lee , J. Mater. Chem. A 2013 , 1 , 2202 – 2210 .

[38] M. A. C. López, L. E. Alarcón, M. Picquart, R. Arroyod, G. Córdoba, E. H. Poniatowski, Opt. Mater. 2011, 33, 480 – 484.

[39] L. Kumari1, Y. R. Ma, C. C. Tsai, Y. W. Lin, S. Y. Wu, K. W. Cheng, Y. Liou, Nanotechnology 2007, 18, 1 - 7.

[40] X. L. Yang, K. C. Fan, Y. H. Zhu, J. H. Shen, X. Jiang, P. Zhao, S. R. Luan, C. Z. Li, ACS Appl. Mater. Interfaces 2013, 5, 997−1002.

[41] D. N. Lan, Y. Y. Chen, P. Chen, X. Y. Chen, X. Wu, X. L. Pu, Y. Zeng, Z. H. Zhu, ACS Appl. Mater. Interfaces 2014, 6, 11839−11845.

[42] J. Park, I. Choi, M. J. Lee, M. H. Kim, T. Lim, K. H. Park, J. Jang, S. M. Oh, S. K. Cho, J. J. Kim, Electrochim. Acta 2014, 132, 338 – 346.

[43] X. Zhang, X. Z. Zeng, M. Yang, Y. X. Qi, Eur. J. Inorg. Chem. 2014, 2, 352 – 356.

[44] D. Galizzioli, F. Tantardini, S. Trasatti, J. Appl. Electrochem. 1974, 4, 57 – 67.

[45] R. G. Gonzalez-Huerta, G. Ramos-Sanchez , P. B. Balbuena, J. Power Sources 2004, 268, 69 - 76.

[46] C. C. L. McCrory, S. Jung, J. C. Peters, T. F. Jaramillo, J. Am. Chem. Soc. 2013, 135, 16977 − 16987.

[47] M. G. Walter, E. L. Warren, J. R. McKone, S. W. Boettcher, Q. Mi, E. A. Santori, N. S. Lewis, Chem. Rev. 2010, 110, 6446 – 6473.

[48] X. J. Liu, Z. Chang, L. Luo, T. H. Xu, X. D. Lei, J. F. Liu, X. M. Sun, Chem. Mater. 2014, 26, 1889 - 1895.

[49] Y. G. Li, P. Hasin, Y. Y. Wu, Adv. Mater. 2010, 22, 1926 - 1929.

[50] B. G. Lu, D. X. Cao, P. Wang, G. L. Wang, Y. Y. Gao, Int. J. Hydrogen Energ. 2011, 36, 72 - 78.

[51] Y. Y. Liang, Y. G. Li, H. L. Wang, J. G. Zhou, J. Wang, T. Regier, H. J. Dai, Nat. Mater. 2011, 10, 780 - 786.

[52] V. K. V. P. Srirapu, C. S. Sharma, R. Awasthi, A. S. K. Singh, Phys. Chem. Chem. Phps. 2014, 16, 7385 - 7393.

[53] M. T. de Groot, M. Merkx, A. H. Wonders, M. T. M. Koper, J. Am. Chem. Soc. 2005, 127, 7579 - 7586.

[54] C.C. L. McCrory, S. Jung, J.C. Peters, T.F. Jaramillo, J. Am. Chem. Soc. 2013, 135, 16977 – 16987.

[55] K. M. Hercule , Q. L. Wei , A. M. Khan , Y. L. Zhao , X. C. Tian , L. Q. Mai. Nano Lett. 2013, 13, 5685 – 5691.

[56] A. S. Baranski, T. Krogulec, L. J. Nelson, P. Norouzi, Anal. Chem. 1998, 70, 2895 - 2901.

[57] S. Mao, Z. H. Wen, T. Z. Huang, Y. Hou, J. H. Chen, Energy Environ. Sci. 2014, 7, 609 – 616.

[58] J. F. Xie, J. J. Zhang, S. Li, F. B. Grote, X. D. Zhang, H. Zhang, R. X. Wang, Y. Lei, B. C. Pan, Y. Xie, J. Am. Chem. Soc. 2013, 135, 17881−17888.

[59] M. Sadakane, C. Takahashi, N. Kato, H. Ogihara, Y. Nodasaka, Y. Doi, Y. Hinatsu, W. Ueda. Bull. Chem. Soc. Jpn. 2007, 80(4), 677 - 685.

[60] C. Y. Chiang, Y. Shin, K. Aroh, S. Ehrman, Int. J. Hydrogen Energ. 2012, 37, 8232 - 8239.

Figure captions:

Figure 1. Schematic illustration of the synthesizing procedures of 3D MoO_2-CoO-Carbon catalyst.

Figure 2. XRD spectra of M200-C-Carbon before and after CoO modification, SEM and TEM images of M200-C-Carbon before (b,d,e) and after CoO modification (c,f,g)

Figure 3. EDS elemental mapping images from TEM for the samples of M200-Carbon and M200-C-Carbon

Figure 4. Raman spectra of M200-Carbon and M200-C-Carbon (a),High-resolution XPS spectrum of the Mo 3d (b), Co 2p (c), C 1s (d), O 1s (e) core level

Figure 5. DTA and TGA curves corresponding to m-MoO_2 transformation in air and N_2 atmosphere.

Figure 6. (a) Experimental linear sweep voltammetry curves of the samples (M200-Carbon, M200-C-Carbon, CoO, Comercial MoO_2, RuO_2 and Ni foam) in 1 M KOH. (b) onset potentials (E_{onset}) and potentials required to reach j=10 mA cm^{-2} ($E_{j=10\ mA\ cm\text{-}2}$) of the OER catalyzed by prepared catalysts; (c)Tafel plots of M200-Carbon, M200-C-Carbon, and RuO_2 at low and high potential region (scan rate 0.5 mV s^{-1}). (d)EIS of M200-Carbon and M200-C-Carbon Inset in (d): the corresponding equivalent circuit diagram consisting of an electrolyte resistance (Rs), a charge-transfer resistance (Rt), and a constant-phase element (CPE). (e) chronopotentiometry curves of M200-Carbon, M200-C-Carbon on Ni foam electrode under high current densities of 10 and 20 mA cm^{-2} ; (f) polarization curvesof M200-C-Carbon before and after 1000 potential cycles

Figure 7. (a) Tafel plots of different samples (M200-Carbon, M400-Carbon, M200-C-Carbon, M400-C-Carbon and RuO_2) at low and high potential region, (b) A plot of turnover frequencies of the different electrodes (M200-Carbon, M400-Carbon, M200-C-Carbon, M400-C-Carbon and RuO_2) evaluated at a overpotential of 0.35 V, (c) onset potentials (E_{onset}) and potentials required to reach j=10 mA cm^{-2} ($E_{j=10\ mA\ cm\text{-}2}$)

of the OER catalyzed by prepared catalysts (M200-Carbon, M400-Carbon, M200-C-Carbon, and M400-C-Carbon),(d) The current density obtained at 1 V (vs Ag/AgCl) in dependence of cycle numbers for various electrocatalysts.